

RESEARCH ARTICLE | JUNE 20 2025


Discharge dynamics of ionization wave manipulated by electrical potential amplitudes in atmospheric pressure plasma jet

Chenzi Lu ; Shaofeng Xu ; Yongfeng Mei ; Gaoshan Huang ; Ying Guo  ; Jianjun Shi  *Appl. Phys. Lett.* 126, 244102 (2025)<https://doi.org/10.1063/5.0271135>

Articles You May Be Interested In


Vibration and rotation temperature distributions optimization of microwave plasma jets in atmospheric pressure

Phys. Plasmas (April 2025)



**Your One-Stop Shop for the
Best Brands in Optics**

- Extensive inventory with over 34,000 products available & 2,900 new products
- Fast shipping from our 9 distribution centres around the globe
- Bringing 80+ years of optical expertise to customers worldwide

 **Edmund**
optics | worldwide

[Shop Now](#)

Discharge dynamics of ionization wave manipulated by electrical potential amplitudes in atmospheric pressure plasma jet

Cite as: Appl. Phys. Lett. **126**, 244102 (2025); doi: [10.1063/5.0271135](https://doi.org/10.1063/5.0271135)

Submitted: 15 March 2025 · Accepted: 29 May 2025 ·

Published Online: 20 June 2025



View Online



Export Citation



CrossMark

Chenzi Lu,^{1,2}  Shaofeng Xu,³  Yongfeng Mei,^{1,2,4}  Gaoshan Huang,^{1,2}  Ying Guo,^{3,a)}  and Jianjun Shi^{1,4,a)} 

AFFILIATIONS

¹Yiwu Research Institute of Fudan University, Yiwu, Zhejiang 322099, People's Republic of China

²Department of Materials Science, International Institute for Intelligent Nanorobots and Nanosystems, Fudan University, Shanghai 200438, People's Republic of China

³College of Science, Donghua University, Shanghai 201620, People's Republic of China

⁴Institute of Optoelectronics, Fudan University, Shanghai 200438, People's Republic of China

^{a)}Authors to whom correspondence should be addressed: guoying@dhu.edu.cn and jianjunshi@gmail.com

ABSTRACT

The auxiliary pulse voltage on the discharge dynamics of ionization wave in atmospheric pressure plasma jet is investigated by both experimental and numerical methods. The distribution of electrical potential is modified by the introduction of auxiliary pulse voltage. The velocity and intensity of ionization wave in terms of plasma bullet is enhanced by reducing the amplitude of auxiliary pulse voltage. The uniformly distributed electron and ion density are obtained by raising the amplitude of auxiliary pulse voltage. By reducing the amplitude of auxiliary pulse voltage, the ion and electron density are concentrated in the ionization wave front, which improves the radial electric field and expands the radial size of plasma bullet. It shows that the electric field, the ion and electron density, and the electron temperature can be enhanced by elevating the amplitude difference between the internal and the applied auxiliary electrical potential.

Published under an exclusive license by AIP Publishing. <https://doi.org/10.1063/5.0271135>

Recent advancements in atmospheric pressure plasma jet (APPJ) technology underscore its extensive potential across a variety of applications. The generation of APPJ employs the dielectric barrier discharge (DBD) method, in which a noble gas flows through a discharge gap to generate and release the plasma into the open air. This process produces a continuous stream of directed ionization wave, which are often visualized as high-speed luminous spots known as “plasma bullets.”^{1–3} These plasma bullets function as powerful chemical reactors, generating reactive species crucial for a range of applications. Notably, APPJ can transmit high electric fields over significant distances, enabling them to impart charges onto remote objects.^{4,5} This capability is particularly beneficial for precise surface modifications, including biological tissues. The ability of APPJ to interact with complex surfaces has attracted considerable scientific and practical interest, although many aspects of their mechanisms and applications remain unresolved. Furthermore, APPJ operated with nanosecond repetitive pulsing has demonstrated the production of substantial reactive species and high-energy electrons, thereby broadening their applicability in

material processing,^{6–8} surface modification,^{9–12} as well as plasma medicine and biochemistry.^{13–17}

In order to expand the application of APPJ, it is necessary to study the generation and propagation mechanisms of the plasma jet and develop manipulation technologies. Many previous studies have demonstrated significant achievements on manipulating plasma jets through external conditions^{4,18–21} and discharge dynamics in propagation of ionization wave.^{20,22–26} In our previous study,²⁷ a noninvasive method was developed to measure the electrical potential in an open environment that played a crucial role in the propagation of plasma bullets. It proposes that enhancements and restrictions could be achieved through different waveforms of auxiliary pulse voltage. Here, the dependence of discharge dynamics on the auxiliary pulse voltage amplitude is studied through both experiment and simulation. The experimental system used to generate the plasma jet is a three-electrodes configuration similar to that described in a previous work²⁷ with three electrodes (One less GND compared to previous work) wrapped on the outer-tube wall, which are the power electrode (PE),

the grounded electrode (GND), and a copper ring with a 0.1 mm width acting as the auxiliary electrode (AE) between the PE and GND. The distance between the PE and GND and that between the PE and AE are 50 and 20 mm, respectively. Similarly, an equivalent 2D numerical simulation model was developed, which includes an air region, copper electrodes, a dielectric region, and an inner discharge area.

Figure 1(a) shows the waveforms of pulsed voltage for both the experiment and simulation. Figure 1(b) illustrates the voltage waveforms applied in the simulation, including the power pulse voltage (black) = 6 kV and the self-consistent electrical potential (EP, red dashes) on the outer-tube wall generated at the axial distance (AD) of 20 mm, where the AE is located. Three types of auxiliary pulse voltage (APV) waveforms are also presented in Fig. 1(b), with amplitudes of APV = 2.0 kV (blue), 4.0 kV (red), and 6.0 kV (orange), which are lower, similar to, and higher than the self-consistent electrical potential of 4.0 kV when ionization wave propagates to AD = 20 mm, respectively. Figure 1(b) illustrates that the self-consistent electrical potential at AD = 20 mm exhibits an immediate increase upon the application of PPV, followed by plasma initiation after a nanosecond delay.

The images comparing between plasma bullet captured by an ICCD camera with a 40 ns exposure time in experiment and He^+ density spatial profile obtained from simulation when APV is 4.0 kV are shown in Figs. 2(I-a1)–2(I-e1) and 2(I-a2)–2(I-e2), respectively. Five

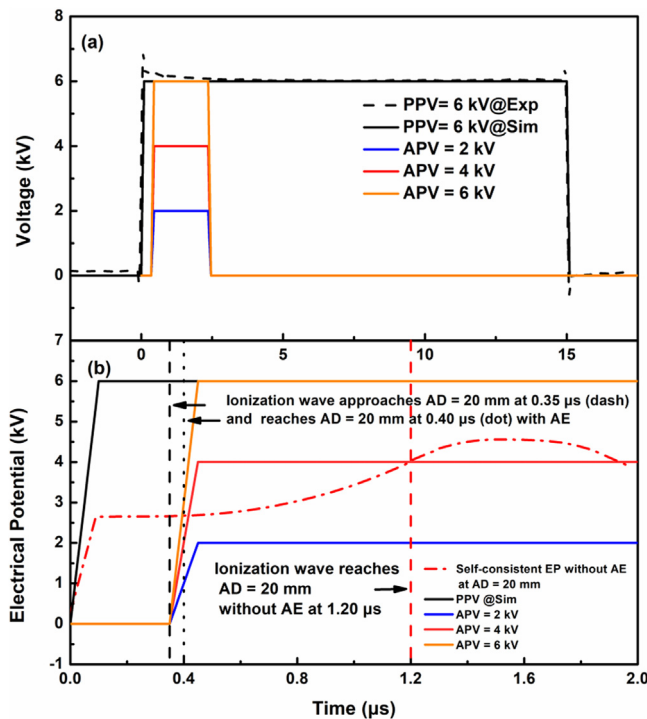


FIG. 1. (a) The waveforms of power pulse voltage in experiment (PPV, black dash) and in simulation (PPV, black) = 6 kV as well as auxiliary pulse voltage (APV) in simulation = 2.0 kV (blue), 4.0 kV (red), and 6.0 kV (orange). (b) The rising phase of waveforms of PPV (black), self-consistent electrical potential (red dash-dot) on the outer-tube wall at axial distance (AD) = 20 mm and APV = 2.0 kV (blue), 4.0 kV (red), and 6.0 kV (orange) in simulation. The auxiliary electrode (AE) is placed in AD = 20 mm.

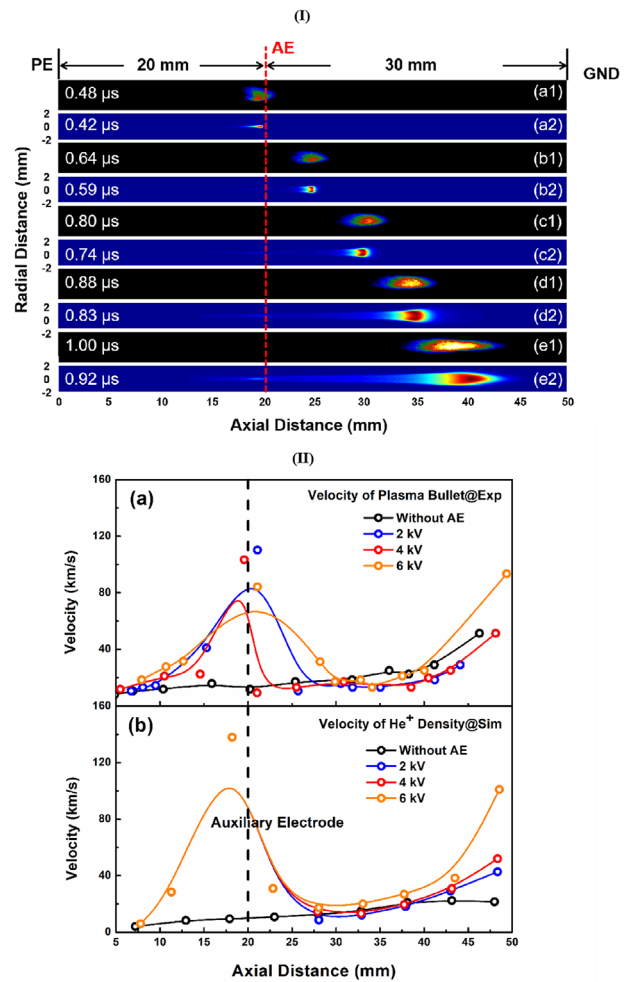


FIG. 2. (I) Comparison figures between (a1)–(d1) plasma bullet images captured by the ICCD camera in experiment with 40 ns exposure time and (a2)–(d2) He^+ density spatial profiles obtained in simulation when plasma bullet propagates to the position of AD = 20, 25, 30, 35, 40, and 45 mm; (II) (a) the velocity of plasma bullet in experiment and (b) velocity of He^+ density in simulation without AE (black) and discharge with APV = 2.0 kV (blue), 4.0 kV (red), and 6.0 kV (orange).

typical time instances as the plasma bullet propagates to the position of AD = 19, 24, 30, 35, 40 mm have been selected. Figures 2(II-a) and 2(II-b) show the velocity of plasma bullets in the experiment and the He^+ density in the simulation, respectively. The velocity of plasma bullet around AD = 20 mm increases to 110.2, 103.4, and 84.2 km/s in discharge with APV = 2.0, 4.0, and 6.0 kV in experiment, respectively, while in simulation, it is 138.0 km/s in all discharge with different APV due to more stable and accurate waveforms. When both the plasma bullet and He^+ density propagate through the AE, the velocity decreases and then undergoes a second acceleration. The sustained APV on the AE contributes significantly to the second acceleration, which occurs during the plateau period of the pulse voltage. The enhancement of He^+ density velocity increases with the APV amplitude from 2.0 to 6.0 kV.

Figure 3(a) illustrates the effect of AE on the electrical potential of the ionization wave front. The introduction of AE with varying amplitudes of APV initially reduces the electrical potential on the ionization wave front from 5.2 to 4.7 kV at the moment of generation. Following a sustained decline in the region between AD = 0 and 20 mm with APV remaining at 0, the electrical potential on the ionization wave front begins to rise at AD = 20 mm from a minimum value of 2.9 kV with an instantaneous increase in APV. The magnitude of this rise in the electrical potential varies with the amplitude of APV applied at the specific time. In discharges with APV = 6.0 kV, the peak electrical potential increases to 6.3 kV, while in discharges with APV = 2.0 kV, which is lower than the self-consistent electrical potential previously observed, it increases to 4.8 kV. These results indicate that introducing AE with an instantly applied APV increases the electrical potential on the ionization wave front. Furthermore, with the location of AE acting as a boundary, the electrical potential can be divided into lower and higher regions.

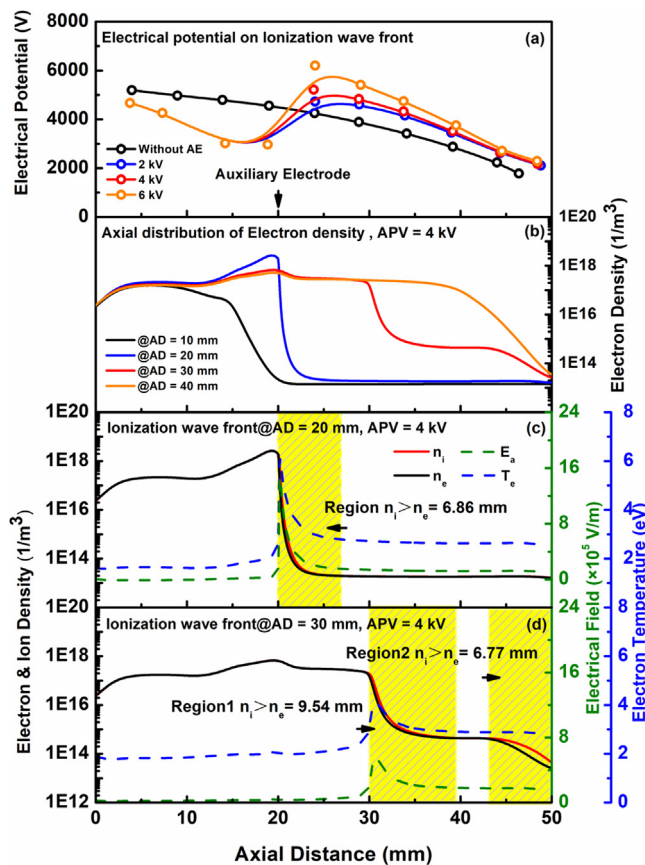


FIG. 3. (a) Electrical potential distribution on the ionization wave front in discharge without AE (black) and discharge with APV = 2.0 kV (blue), 4.0 kV (red), and 6.0 kV (orange) and (b) axial distribution of electron density in discharge with APV = 4.0 kV when ionization wave propagates to the positions of AD = 10 (black), 20 (blue), 30 (red), and 40 (orange) mm; the axial distribution when ionization wave propagates to the position of AD = 20 (c) and 30 mm (d) including ion density (red), electron density (black), axial electrical field (green dash), and electron temperature (blue dash) in discharge with APV = 4.0 kV.

Figure 3(b) shows the axial distribution of electron density in discharge with APV = 4.0 kV. An enhancement in the electron density is observed at AD = 20 mm where AE is applied. When ionization wave initially generates near the power electrode and propagates close to AD = 10 mm, the electron density in the region between AD = 10 and 20 mm increases due to the lower electrical potential in AE. As the ionization wave propagates to AD = 20 mm, the electron density in discharge with APV = 4.0 kV is $1.4 \times 10^{18} \text{ m}^{-3}$ and it increases to $3.4 \times 10^{18} \text{ m}^{-3}$ with the APV amplitude decreasing from 6.0 to 2.0 kV, which is higher than the electron density of $1.1 \times 10^{17} \text{ m}^{-3}$ in the discharge without AE at the same position. Furthermore, the electron density in regions not yet propagated by the ionization wave remains low, below 10^{14} m^{-3} , in discharges with AE. These results demonstrate that introducing AE concentrates the electron density within the ionization wave front and the regions it has propagated to, while restricting the accumulation of electron density in regions where ionization wave has not yet approached. Additionally, even after the ionization wave have moved away from AE, a higher magnitude of electron density persists in the regions surrounding AE.

Figures 3(c) and 3(d) show the axial distribution of electron density, ion density, electrical field, and electron temperature when ionization wave propagates to positions AD = 20 mm (c) and AD = 30 mm (d) in discharge with APV = 4.0 kV, where the former is wrapped by AE and the latter is away from AE, respectively. The peak values of the axial electrical field and electron temperature correspond to the maximum gradient of the electron and ion density profiles. A region is present on the ionization wave front where ion density exceeds electron density. The width of this region in the discharge without AE is 12.86 mm, which reduces to 6.86, 4.88, and 9.88 mm in discharge with APV = 2.0, 4.0, and 6.0 kV, respectively. These results indicate that APV increases the gradient of electron and ion density on the ionization wave front and reduces the width of the region where ion density exceeds electron density. Additionally, the distribution of electron and ion density correlates with the distribution of the electrical field. As shown in Fig. 3(c) with the green dash line, the peak value of the axial electrical field in the discharge with APV = 4.0 kV is $1.5 \times 10^6 \text{ V/m}$, while in discharge without AE and discharges with APV = 2.0 and 6.0 kV, the axial electrical field values are 2.8×10^5 , 1.8×10^6 , and $6.2 \times 10^5 \text{ V/m}$, respectively. Introducing AE increases the peak value of the electrical field on the ionization wave front, but this value decreases as APV increases. Furthermore, the axial distribution of electron temperature, shown in Fig. 3(c) with the blue dash line, reveals peak values of 3.29, 6.45, 6.06, and 4.28 eV for the discharge without AE and with APV = 2.0, 4.0, and 6.0 kV, respectively. Figure 3(d) shows the axial distributions of electron density, ion density, electron temperature, and electrical field when ionization wave propagates to the position of AD = 30 mm, which is away from AE in discharge with APV = 4.0 kV. The peak value of the axial electrical field and electron temperature at this moment are all lower than those at AD = 20 mm. Additionally, the region where ion density exceeds electron density on the ionization wave front expands to 9.39, 9.54, and 9.74 mm in discharge with APV = 2.0, 4.0, and 6.0 kV, respectively, with an additional region showing similar characteristics near GND. In the discharge without AE, these two regions are connected, resulting in a combined width of 20.11 mm, which is similar in discharge with APV = 6.0 kV.

Figures 4(a) and 4(b) illustrate the radial distribution of electron density, ion density, radial electrical field, and electron temperature

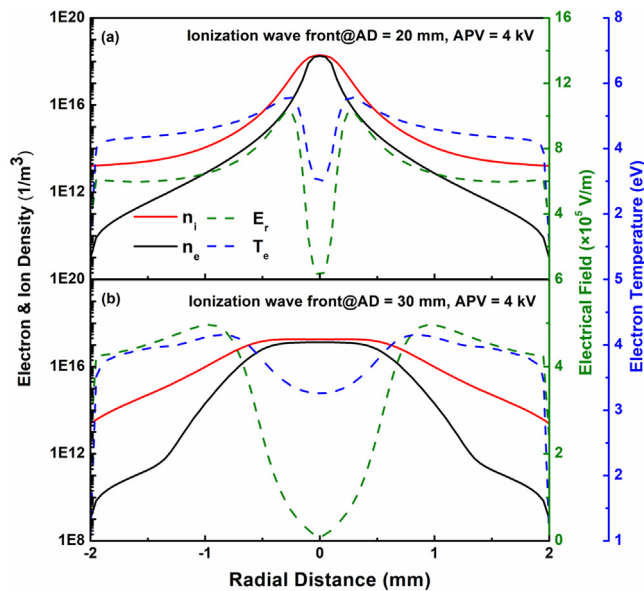


FIG. 4. The radial distribution when ionization wave propagates to the position of AD = 20 (a) and 30 mm (b) including ion density (red), electron density (black), radial electrical field (green dash), and electron temperature (blue dash) in discharge with APV = 4.0 kV.

when ionization wave propagates to positions AD = 20 and AD = 30 mm. When ionization wave is propagating through AE with APV = 4.0 kV, the distributions of electron and ion density become more concentrated at the ionization wave front, and higher peak values of electron temperature and radial electrical field are observed on both sides, decreasing toward the discharge tube wall. With increasing APV, the electron and ion density on both sides of the ionization wave front become more similar. The peak values of the radial electrical field are 1.2×10^6 , 1.0×10^6 , and 4.0×10^5 V/m for APV = 2.0, 4.0, and 6.0 kV, respectively, while the peak values of electron temperature are 5.79, 5.58, and 4.45 eV for APV = 2.0, 4.0, and 6.0 kV, respectively. However, in discharge without AE, the radial electrical field and electron temperature are relatively low, with peak values of 2.7×10^5 V/m and 3.33 eV, respectively, and the distributions are uniform near the inner wall of the discharge tube. Furthermore, when ionization wave propagates to AD = 30 mm, as shown in Fig. 4(b), both electron temperature and radial electrical field are weakened. These distributions are similar between the discharge without AE and those with APV = 6.0 kV.

According to Figs. 1(b) and 3(a), the electrical potential difference ($\Delta\phi$) between the ionization wave front and AE, influenced by APV with varying amplitudes, is 0.4 kV in the discharge without AE and 2.8, 1.2, and 0.3 kV in discharges with APV = 2.0, 4.0, and 6.0 kV, respectively. The characteristics of ionization waves are influenced by $\Delta\phi$. When APV is reduced to 2 kV, $\Delta\phi$ is 2.8 kV establishing a strong axial electric field, driving electron acceleration and ionization front enhancement with increased higher electron density and particle concentration. Conversely, a higher APV = 6.0 kV reduces $\Delta\phi$ to 0.3 kV, which is similar to 0.4 kV in discharge without AE, redistributing spatial charge uniformly and reducing wave front gradients of electron

and ion density. Additionally, the region where ion density exceeds electron density on the ionization wave front is a structure similar to sheath near cathode, which here is regarded as “transient dynamic ionization sheath” caused by axial electric field at the ionization wave front propels accelerated electron ejection, resulting in transient localized charge separation. This result is similar to previous study describing the ionization wave front as a virtual cathode.²⁸ The thickness of transient dynamic ionization sheath narrows to with the decrease in the APV amplitude, concentrating spatial charge distribution and amplifying electrical field on the ionization wave front.

Figure 5(a) presents the distribution of radial electrical potential when ionization wave propagates to AD = 30 mm, as obtained in simulation. Figure 5(b) illustrates the full width at half maximum (FWHM) of the plasma bullet captured experimentally by the ICCD camera, along with the radial electrical potential in the discharge without AE and with APV = 2.0, 4.0, and 6.0 kV, at selected RD of ± 0.25 , ± 0.65 , and ± 1.40 mm. The FWHM is employed to describe the radial size of the plasma bullet. The FWHM (black dash-dot line) of the plasma bullet exhibits a similar trend compared to the radial electrical field at RD = ± 0.65 mm. At AD = 30 mm, the FWHM of the plasma bullet is 3.18 mm with a low radial electrical field of 0.6×10^5 V/m in the discharge without AE. Conversely, the FWHM in the discharge

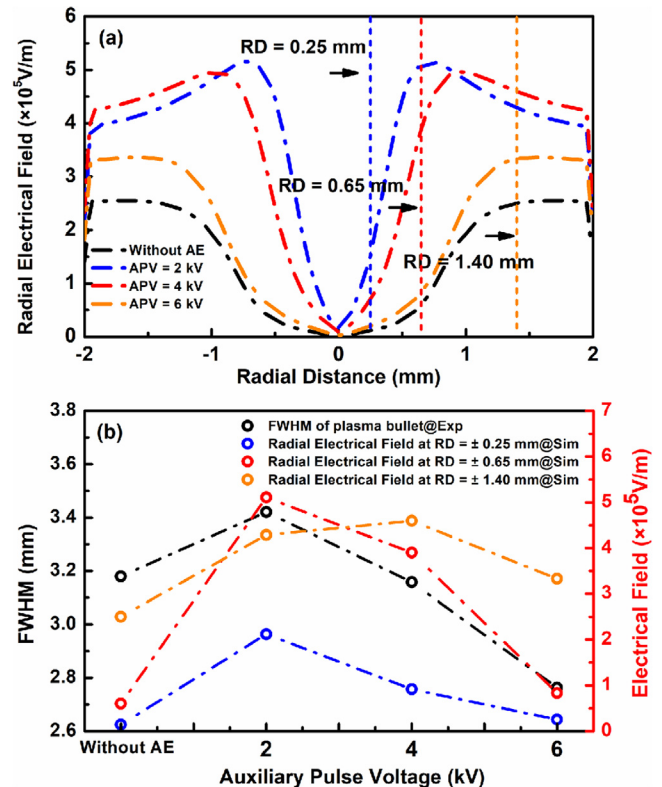


FIG. 5. (a) The radial distribution of radial electrical field in discharge without AE (black) and discharge with APV = 2.0 kV (blue), 4.0 kV (red), and 6.0 kV (orange); (b) the FWHM of plasma bullets and radial electrical field obtained from RD = ± 0.25 mm (blue), ± 0.65 mm (red), and ± 1.40 mm (orange) in discharge without AE and APV = 2.0, 4.0, and 6.0 kV.

with APV = 2.0 kV is 3.42 mm, associated with a higher radial electrical field of 5.1×10^5 V/m. As the APV increases from 2.0 to 6.0 kV, the FWHM of the plasma bullet decreases from 3.42 to 2.76 mm, while the radial electrical field decreases from 5.1×10^5 to 0.8×10^5 V/m. According to Fig. 4, the introduction of APV will lead to the enhancement of current path bifurcation of dual pathways, which are axial propagation via the ionization front and radial transport along the plasma–gas interface as stronger radial fields promote lateral charge spreading. This result indicates that the radial electrical field significantly influences the radial size of the plasma bullet.

In summary, the impact of auxiliary pulse voltage (APV) on the discharge dynamics of the plasma bullet in atmospheric pressure plasma jet (APPJ) is studied using both experimental and numerical simulation methods. It demonstrates that the velocity and intensity of ionization wave in terms of plasma bullet are enhanced by reducing the amplitude of APV. The introduction of an auxiliary electrode (AE) and APV increases the electrical potential on the ionization wave front, and electrical potential difference ($\Delta\phi$) between the ionization wave front and outer-tube wall is manipulated by APV. The electrical field, ion and electron density, the density gradient on the ionization wave front, and electron temperature are increased by raising $\Delta\phi$. Higher APV raises the electrical potential in the discharge region but reduces electron density and temperature between the AE and the grounded electrode. Additionally, radial distributions indicate that more concentrated ion and electron density on the ionization wave front and a higher radial electrical field is obtained by reducing the amplitude of APV. The high radial electrical field at a lower APV expand the radial size of the plasma bullet. The introduced APV provides a method to manipulate the intensity of active species such as N_2^+ and O. These results offer valuable insight into the manipulation of APPJ performance for various applications.

See the [supplementary material](#) for figures including the axial and radial distribution of ion and electron density, electrical field and electron temperature in discharges with APV = 0.0, 2.0, 6.0 kV, the schematic of experiment setup and simulation model, and the intensity of active species manipulated by modified APV.

This work was funded by the Natural Science Foundation of China (12475259, 12175036, and 11875104).

AUTHOR DECLARATIONS

Conflict of Interest

The authors have no conflicts to disclose.

Author Contributions

Chenzi Lu: Data curation (lead); Methodology (equal); Validation (lead); Writing – original draft (lead). **Shaofeng Xu:** Data curation (equal); Software (equal); Supervision (equal). **Yongfeng Mei:** Funding acquisition (lead); Resources (lead); Supervision (lead). **Gaoshan Huang:** Formal analysis (equal); Resources (equal); Supervision (equal). **Ying Guo:** Funding acquisition (lead); Project administration (lead); Supervision (lead). **Jianjun Shi:** Conceptualization (equal); Formal analysis (equal); Funding acquisition (equal); Methodology (equal); Project administration (equal); Resources (equal); Supervision (equal); Writing – review & editing (equal).

DATA AVAILABILITY

The data that support the findings of this study are available from the corresponding authors upon reasonable request.

REFERENCES

- ¹M. E. Pinchuk, Z. Chen, and O. M. Stepanova, “Transition from one-pass mode to stepwise propagation of a guided streamer along a helium plasma jet,” *Appl. Phys. Lett.* **119**(5), 054103 (2021).
- ²M. Teschke, J. Kedzierski, E. G. Finantu-Dinu, D. Korzec, and J. Engemann, “High-speed photographs of a dielectric barrier atmospheric pressure plasma jet,” *IEEE Trans. Plasma Sci.* **33**(2), 310–311 (2005).
- ³J. L. Walsh, J. J. Shi, and M. G. Kong, “Contrasting characteristics of pulsed and sinusoidal cold atmospheric plasma jets,” *Appl. Phys. Lett.* **88**(17), 171501 (2006).
- ⁴M. E. Pinchuk, O. M. Stepanova, M. Gromov, C. Leys, and A. Nikiforov, “Variation in guided streamer propagation along a DBD plasma jet by tailoring the applied voltage waveform,” *Appl. Phys. Lett.* **116**(16), 164102 (2020).
- ⁵E. Karakas, M. A. Akman, and M. Laroussi, “The evolution of atmospheric-pressure low-temperature plasma jets: Jet current measurements,” *Plasma Sources Sci. Technol.* **21**(3), 034016 (2012).
- ⁶T. Hato, K. Nitta, H. Muneoka, Y. Shimizu, K. Terashima, and T. Ito, “Synthesis of ZnO and ZnO/Ag fine particles by plasma-assisted inkjet processing,” *J. Phys. D: Appl. Phys.* **57**(31), 315203 (2024).
- ⁷S. Agrotis, M. E. Sener, O. S. J. Hagger, A. D. Handoko, and D. J. Caruana, “One-step synthesis of nanosized Cu-Ag films using atmospheric pressure plasma jet,” *Appl. Mater. Today* **39**, 102286 (2024).
- ⁸M. G. Neira-Velazquez, J. de, J. Ku-Herrera, R. I. Narro-Céspedes, S. E. Flores-Villasenor, Y. L. Cortez-Garza, C. G. Cuellar-Gaona, and G. Soria-Arguello, “Carbon nanostructures synthesis by catalyst-free atmospheric pressure plasma jet,” *J. Phys. -Appl. Phys.* **57**(31), 315302 (2024).
- ⁹C. Zhang, Z. Fan, and R. Sang, “Effect of plasma modification on UV-curable ink-jet coating on medium-density fiberboard (MDF),” *Wood Mater. Sci. Eng.* **2024**, 1–10.
- ¹⁰X. Kong, H. Li, W. Yang, S. Li, D. Yang, W. Ning, and R. Wang, “Atmospheric pressure plasma jet impinging on fiber arrays: Penetration pattern determined by fiber spacing,” *Appl. Phys. Lett.* **122**(8), 084101 (2023).
- ¹¹M. Chen, X. Dong, K. Wu, J. Ran, P. Jia, J. Wu, and X. Li, “A large-scale filament-free planar plume generated by an argon plasma jet in a gas-confined barrier discharge geometry,” *Appl. Phys. Lett.* **124**(21), 214102 (2024).
- ¹²J. Jiao, W. Xia, J. Wu, B. He, H. Tian, Y. Liu, and G. Xu, “Effect of oxygen on the discharge characteristics of argon doped ethanol plasma jet and its application in surface modification of polyimide films,” *Plasma Sources Sci. Technol.* **33**(9), 095002 (2024).
- ¹³J. Polito and M. J. Kushner, “A hierarchical model for bacterial cell inactivation in solution by direct and indirect treatment using cold atmospheric plasmas,” *J. Phys. D: Appl. Phys.* **57**(40), 405207 (2024).
- ¹⁴K. Stapelmann, B. Myers, M. H. Quesada, E. Lenker, and P. J. Ranieri, “Following O and OH in He/O₂ and He/H₂O gas mixtures-from the gas phase through the liquid phase to modifications on a biological sample,” *J. Phys. D: Appl. Phys.* **54**(43), 434003 (2021).
- ¹⁵S. Puri, S. K. Mandal, N. K. Sharma, P. Pal, R. P. Lamba, V. Miller, U. N. Pal, and P. R. Deepa, “Biochemical evaluation of wound healing efficacy of cold plasma-conditioned media under different operational conditions,” *J. Phys. D: Appl. Phys.* **57**(40), 405201 (2024).
- ¹⁶K. C. S. Kumar, A. L. K. Derrick-Roberts, S.-H. Hong, B. Ghimire, J.-S. Oh, and E. J. Szili, “Influence of duty cycle on the physicochemical characteristics of an AC-driven argon plasma jet and its impact on hydrogen peroxide production and cell viability,” *J. Phys. Appl. Phys.* **57**(37), 375208 (2024).
- ¹⁷M. Chen, J. Chen, T. Xie, Z. Chen, and G. Xu, “Effects of cold atmospheric plasma-treated medium on HaCaT and HUVEC cells in vitro,” *PLASMA Process. Polym.* **21**, e2400132 (2024).
- ¹⁸M. E. Pinchuk, O. M. Stepanova, A. M. Astafiev, A. V. Lazukin, and Z. Chen, “Stepwise propagation of a guided streamer along a DBD helium plasma jet fed by biased oscillating voltage,” *Appl. Phys. Lett.* **114**(19), 194103 (2019).

- ¹⁹P. Olszewski, E. Wagenaars, K. McKay, J. W. Bradley, and J. L. Walsh, "Measurement and control of the streamer head electric field in an atmospheric-pressure dielectric barrier plasma jet," *Plasma Sources Sci. Technol.* **23**(1), 015010 (2014).
- ²⁰G. V. Naidis and J. L. Walsh, "The effects of an external electric field on the dynamics of cold plasma jets—experimental and computational studies," *J. Phys. D: Appl. Phys.* **46**(9), 095203 (2013).
- ²¹Q. Han, Y. Guo, Y. Zhang, J. Zhang, and J. Shi, "Enhancement of radio frequency plasma plume by pulsed plasma bullet at atmospheric pressure," *Appl. Sci.* **12**(11), 5430 (2022).
- ²²B. Huang, C. Zhang, W. Zhu, X. Lu, and T. Shao, "Ionization waves in nanosecond pulsed atmospheric pressure plasma jets in argon," *High Volt.* **6**(4), 665–673 (2021).
- ²³D. Peng, Y. Fu, R. Zhang, and L. Wang, "Evolution of solid-in-hollow structured plasma bullet: Modulated by pulse repetition frequency and rising time," *Appl. Phys. Lett.* **124**(13), 134101 (2024).
- ²⁴D. Tereshonok, N. Y. Babaeva, G. Naidis, A. G. Abramov, and A. Ugryumov, "Modeling of ionization waves in atmospheric-pressure argon in a long gap," *IEEE Trans. Plasma Sci.* **50**(3), 580–586 (2022).
- ²⁵A. M. Lietz, E. Barnat, J. E. Foster, and M. J. Kushner, "Ionization wave propagation in a He plasma jet in a controlled gas environment," *J. Appl. Phys.* **128**(8), 083301 (2020).
- ²⁶O. Gazeli, C. Lazarou, G. Niu, C. Anastassiou, G. E. Georgiou, and J. Franzke, "Propagation dynamics of a helium micro-tube plasma: Experiments and numerical modeling," *Spectrochim. Acta Part B* **182**, 106248 (2021).
- ²⁷C. Lu, J. Fang, S. Xu, Y. Guo, and J. Shi, "Manipulating the propagation of ionization wave by pulsed electrical potential in atmospheric plasma jet," *Appl. Phys. Lett.* **123**(11), 114104 (2023).
- ²⁸B. L. Sands, S. K. Huang, J. W. Speltz, M. A. Niekamp, J. B. Schmidt, and B. N. Ganguly, "Dynamic electric potential redistribution and its influence on the development of a dielectric barrier plasma jet," *Plasma Sources Sci. Technol.* **21**(3), 034009 (2012).